1   **Revision 3**

2   **Z-contrast imaging and *ab initio* study on "*d*" superstructure in sedimentary**

3   **dolomite**

4   Zhizhang Shen[1], Hiromi Konishi[1], Izabela Szlufarska[2], Philip E. Brown[1], and Huifang Xu[1*]

5

6   [1] NASA Astrobiology Institute, Department of Geoscience,

7   University of Wisconsin - Madison

8   Madison, Wisconsin 53706

9   [2] Department of Materials Science and Engineering,

10   University of Wisconsin-Madison,

11   Madison, Wisconsin 53706

12

13

14   * Corresponding author: Dr. Huifang Xu

15   Department of Geoscience,

16   University of Wisconsin-Madison

17   1215 West Dayton Street, A352 Weeks Hall

18   Madison, Wisconsin 53706

19   Tel: 1-608-265-5887

20   Fax: 1-608-262-0693

21   Email: hfxu@geology.wisc.edu

22

ABSTRACT

24 Nano-precipitates with tripled periodicity along the c-axis are observed in a Ca-rich dolomite

25 sample from Proterozoic carbonate rocks with "molar tooth" structure. This observation is

26 consistent with previous description of d reflections. High-angle annular dark-field STEM

27 imaging (or Z-contrast imaging) that avoids dynamic diffraction as seen in electron diffraction

28 and high-resolution TEM imaging modes, confirms that d reflections correspond to nanoscale

29 precipitates aligned parallel to (*001*) of the host dolomite. The lamellae precipitates have a cation

30 ordering sequence of Ca-Ca-Mg-Ca-Ca-Mg along the c direction resulting in a chemical

31 composition of $Ca_{0.67}Mg_{0.33}CO_3$. This superstructure is attributed to the extra or d reflections,

32 thus is referred to as the d superstructure in this study. The structure can be simply described as

33 interstratified calcite/dolomite. The crystal structure of the d superstructure calculated from

34 density functional theory (DFT) has a space group of *P31c* and has a and c unit cell parameters

35 of 4.879 Å and 16.260 Å, respectively, values between those of dolomite and calcite. The

36 detailed structural characteristics and parameters obtained from *ab initio* calculations are also

37 reported in this paper. The method of combining Z-contrast imaging and *ab initio* calculation can

38 be used for solving structures of other nano-precipitates and nano-phases.

39

40 **INTRODUCTION**

41 The dolomite($R\bar{3}c$) structure has alternating Ca^{2+} and Mg^{2+} cation layers along the **c**-axis with

42 the triangular CO_3^{2-} anion layers lying between two cation layers. Since the size of Mg^{2+} ions is

43 smaller than that of Ca^{2+}, the CO_3^{2-} layers are closer to Mg^{2+} layers. The lack of c glides in the

44 dolomite structure due to the cation ordering causes the occurrence of extra reflections (*b*

45 reflections, $h\bar{h}0l$, *l*= odd) in dolomite diffraction patterns compared to that of calcite (*a*

46 reflections only) (Reeder, 1992). Two additional reflections (*c* and *d* reflections) have been

47 observed in natural sedimentary dolomite. Previously reported *c* reflections were interpreted as

48 being a result of cation ordering within dolomite basal planes (Van Tendeloo et al., 1985). Our

49 recent STEM work confirmed that the "*c*"-reflections could result from multiple diffraction

50 between the host dolomite and twinned Mg-calcite nano-lamellae under TEM imaging and

51 diffraction modes (Shen et al., 2013). The *d* reflection was first observed in Devonian dolomite

52 samples by Wenk and Zenger (1983) and have been also found in ankerite samples (Rekesten,

53 1990). The *d* reflections occur as satellites around *a* and *b* reflections with diffraction vector ~1/3

54 (000l)* and are usually streaking along *c** direction (Wenk and Zenger,1983; Wenk and Zhang,

55 1985; Van Tendeloo et al., 1985).

56

57 Dynamical diffraction in transmission electron microscopy (TEM) mode has been a major

58 problem for structure determination as shown in previous work of analyzing "*c*" superstructures

59 (Shen et al., 2013). The scanning transmission electron microscopy (STEM) method uses the

60 high-angle annular dark-field (HAADF) detector to give the most highly localized 1s Bloch state

61 imaging, which eliminates most of the obvious effects of dynamical diffraction (Pennycook,

62   2002). With the advantage of a spherical aberration corrector, the resolution of HAADF STEM

63   or Z-contrast images is only limited by the size of the 1s Bloch state that is ~0.6-0.8 Å

64   (Pennycook et al., 2000). The intensity of Z-contrast images is dependent on the atomic number

65   of atoms through the $\sim Z^2$ dependence of the Rutherford scattering cross-section, which thus

66   provides chemical information for the material (Kirkland, 1998; Pennycook et al., 2000). A study

67   of microstructures in natural dolomite samples using Z-contrast images may help find answers to

68   previous observations of superstructures and explore new microstructures in dolomite.

69

70   In addition to experimental studies in mineralogy, the application of *ab initio* calculations of

71   crystal structure, phase stability, and physical properties of minerals at given pressure and

72   temperature has increased in the past few years (Ogonov et al., 2006; Barnard and Xu, 2008;

73   Chatterjee and Saha-Dasgupta, 2010; Stackhouse et al., 2010). Density functional theory (DFT)

74   uses the functional of electron density to solve the Schrödinger equation for a many electron

75   system to acquire the minimum energy of the system (Scholl and Steckel, 2009). This method

76   can calculate the enthalpy of a system at 0K and the corresponding structure. Since STEM work

77   only provides topological information for the crystal structure, the use of the DFT method is

78   needed in this study to calculate the detailed crystal structure of the *d* phase and confirm our

79   model for the *d* superstructure by comparing the energetic stability of our model to another

80   model proposed in literature.

81

82   The "molar tooth" structure refers to vertical and horizontal ribbons and blobs of fine-grained

83   calcite in a dolomite host (Bauerman, 1885). This structure has only been recognized in

84   Mesoproterozoic and Neoproterozoic marine carbonate rocks with a few exceptions (Frank and

85   Lyons, 1998). The origin and the temporally limited occurrence of molar tooth carbonate have

86   bewildered geologists for over a century (James et al., 1998; Pratt, 1998; Meng and Ge, 2002;

87   Marshall and Anglin, 2004; Pollock et al., 2006; Long, 2007; Kuang et al., 2012). However, no

88   previous work on the nano-scale mineralogy of carbonates with the "molar tooth structure" has

89   been conducted. In this present study, STEM imaging and DFT calculations were combined to

90   provide a complete crystallographic description of the *d* superstructure.

91

92   **SAMPLES**

93   The "molar tooth" carbonate samples were collected near Hungry Horse Dam, Montana, from

94   outcrops of the Helena Formation of the Mesoproterozoic Belt Group (Frank and Lyons, 1998).

95   The sample HHL-00H was chosen for STEM analysis. In the hand specimen of HHL-00H

96   (Figure 1), the thin sinuous vertical and horizontal ribbons with width of ~0.2-1.5cm intersect

97   each other. The "molar tooth" is composed of clean and fine-grained calcite crystals with similar

98   size (~10 μm). The "molar tooth" host has three major phases: dolomite, calcite, and quartz

99   (Figure 2). K-feldspar, illite, chlorite, rutile, and apatite are also present in the "molar tooth" host

100   rock. The XRD powder analysis of the "molar tooth" host rock shows that the dolomite is cation-

101   ordered with the presence of sharp (105) and (009) peaks. The dolomite has a composition of

102   ~$Ca_{1.02}Mg_{0.98}(CO3)2$ based on the d_{104} value (2.890Å) and the relationship between d_{104} values

103   and $MgCO_3$ content in ordered dolomite (Goldsmith and Graf, 1958; Zhang et al., 2010).

104

105   **METHODS**

106   Specimens for STEM measurements were prepared by ion milling. Ion milling was performed

107   with a Fischione 1010 ion mill operated at an accelerating voltage of 4 kV and an incident ion-

108   beam angle of 10°, followed by gentler milling at an accelerating voltage of 2.6 kV and an

109   incident angle of 10° in order to reduce surface amorphous material. The ion-milled samples

110   were lightly carbon coated. The microstructures in the dolomite crystals were examined by using

111   a spherical aberration-corrected FEG- STEM (Titan 80-200) operating at 200 kV at the

112   University of Wisconsin-Madison. This instrument can image single atoms with ~ 0.1 nm or

113   better spatial resolution in STEM mode. Probe current was set at 24.5 pA. Camera length for the

114   image acquisition was set at 160 mm. Collection angle of the HAADF detector for acquiring the

115   Z-contrast images ranges from 54 to 270 milliradians (mrads).

116

117   The DFT calculations were performed by using the Vienna *ab initio* simulation package (VASP)

118   (Kresse et al., 1996). The general gradient approximation (GGA) with the Perdew, Burke, and

119   Ernzerhof (PBE) parameters was employed (Perdew et al., 1996). The projector-augmented wave

120   (PAW) method with an energy cutoff of 600 eV was used. A conventional hexagonal supercell

121   of calcite derived structures including 30 atoms or 6 chemical formula units was used. We tested

122   k-point convergence and a mesh of $3\times3\times1$ was found to be sufficient for the system. Two

123   starting structures for the *d* phase: one with calcite's unit cell parameters from experiments

124   (Graf, 1969) and another with dolomite's (Beran and Zemann, 1977). All the initial structures

125   were optimized using the static energy minimization scheme, where both the shape and volume

126   of the cell were allowed to relax. The structure with minimum energy calculated from the

127   previous step was further calculated by *ab initio* molecular dynamics simulations at 10K to better

128   explore the local minimum. The powder and electronic diffraction patterns of calculated

129   structures were generated by CrystalDiffract$^®$ and SingleCrystal^{TM} respectively.

130

131   **HIGH-RESOLUTION (S)TEM OBSERVATIONS**

132   In TEM images, the modulated microstructures with strong strain contrast are prevalent through

133   the "molar tooth" host dolomite. Calcite inclusions that are a common phenomenon in

134   sedimentary dolomites can be easily recognized because of being free of modulations (Figure 3).

135   Diffuse streaks along $c*$ occur in the electron diffraction pattern of the host dolomite (Figure 4).

136   Some maxima of the streaks are about one third of d^*_{006} (Fig. 4, and also see diffraction patterns

137   of Wenk and Zenger, 1983; Wenk and Zhang, 1985). According to the Fast Fourier Transform

138   (FFT) patterns of different areas in the dolomite images, the streaks in the diffraction pattern

139   come from the precipitates with linear features that are parallel to (001$)$ (Figure 5). However, the

140   precipitates themselves are arranged in such a way that they are roughly parallel to $(1\bar{1}4)$. The

141   observations above match the features of d reflections that were first described by Wenk and

142   Zenger (1983). It was proposed that the streaks parallel to $c*$ could be from stacking disorder

143   (Van Tendeloo et al., 1985).

144

145   The dark areas of the precipitates in the bright field (BF) image under STEM mode become

146   bright areas in the HAADF image (Figure 6), which suggests higher Ca contents in the

147   precipitates than the host dolomite. The occurrence of d reflections in the FFT pattern of the

148   HAADF image excludes the possibility that they are caused by multiple diffraction. In the

149   HAADF of high magnification or Z-contrast image (Figure 7), the alternating bright and dark

150   layers along *c* axis represent the alternating Ca and Mg layers in the normal dolomite structure.

151   However, the *d* dolomite precipitate has the cation sequence of Ca-Ca-Mg-Ca-Ca-Mg- (Figure

152   7). The FFT pattern of this domain shows that the *d* reflections are attributed to this

153   superstructure. This observation is different from the previous model for the *d* superstructure in

154   which every third Mg layer is replaced by a Ca layer producing a sequence of Ca-Mg-Ca-Ca-Ca-

155   Mg- (Wenk and Zhang, 1985). But both sequences produce the same chemical stoichiometry of

156    $Ca_{0.67}Mg_{0.33}CO_3$. However, the repetition along the *c*-axis is doubled in the previous model with

157   respect to the observed Ca-Mg ordering in the Z-contrast image (Figure 7).

158

159   Mg-bearing calcite precipitates are also observed in the dolomite (Figure 8). Along the $(\bar{1}02)$

160   trace, the calcite exsolution region has six consecutive Ca layers as opposed to the dolomite host

161   that has alternating Ca and Mg layers. In the line profile of the calcite region, some Ca columns

162   have slightly lower intensities than the pure Ca columns in the dolomite host, which suggests the

163   existence of a small amount of Mg in this calcite precipitate (Figure 8). This calcite exsolution is

164   similar to Mg-calcite precipitates in Ca-rich dolomite (Shen et al., 2013).

165

166   **DFT CALCULATIONS**

167   The structural parameters for the optimized *d* superstructure from DFT calculations are listed in

168   Table 1. Tables 2 and 3 compare the calculated lattice parameters of dolomite and calcite

169   structures with the reported experimental data. The calculated equilibrium volumes for both

170   dolomite and calcite are slightly smaller than the reported data, the underestimation of the *c*

171   parameter being the major contribution, but are still within the range of previous theoretical

172   calculation data (see Table 2 and 3). The calculated values are for the structures at 0K. The

173   reported experimental values were measured at ambient environment. Temperature could be a

174   factor for the small discrepancy between calculated and measured the unit cell volumes. A small

175   discrepancy between calculated and experimental values of lattice parameters is not uncommon

176   for DFT calculations and may result from the use of an approximate exchange-correlation

177   potential (Hossain et al., 2011). In spite of this discrepancy, the trend found in experimental data

178   is maintained in our DFT calculations. The calculated d superstructure has an $\boldsymbol{a}$ parameter close

179   to that of dolomite but has a $\boldsymbol{c}$ parameter closer to stoichiometric calcite. This finding is

180   consistent with the observation from the diffraction patterns of the d superstructure that the

181   difference between $\boldsymbol{a}$ parameters of dolomite and the d superstructure is smaller than that

182   between $\boldsymbol{c}$ parameters, even though the DFT calculations are unconstrained bulk structure

183   calculations. This trend is reasonable because superstructure precipitates share the (001) interface

184   with the host dolomite. Smaller differences in the $\boldsymbol{a}$ dimensions between the host dolomite and d

185   superstructure would cause less strain at the interface.

186

187   The C-O bonds in CO_3^{2-} groups are rigid and the C-O distances in both experimental and

188   calculation data are constant no matter what the actual composition of the carbonate mineral is. It

189   is interesting to note that the C-O distances in the d superstructure are divided into two categories

190   (Table 1): 1.294Å when a CO_3^{2-} layer is between Ca^{2+} and Mg^{2+} layers along the c axis; and

191   1.297Å when a CO_3^{2-} layer is in between two Ca^{2+} layers. DFT calculations predict slightly

192   shorter Ca-O and Mg-O bonds in dolomite and calcite than experimental data (Table 2 and 3).

193   The Mg-O distance in the d superstructure increases from 2.069Å in calculated dolomite to 2.085

194   Å. The Ca-O distance in the d superstructure differs depending on the oxygen positions; the Ca-

195   O distances (2.374 Å) are larger when the oxygen ions are from CO_3^{2-} group sitting in between

196   Ca^{2+} and Mg^{2+} layers than those (2.355 Å) from CO_3^{2-} group between two Ca^{2+} layers. This is

197   because that the CO_3^{2-} layers are closer to Mg^{2+} layers than Ca^{2+} layers due to the smaller Mg^{2+}

198   radius. The inversion center is missing in the *d* superstructure while the c glide is retained. The

199   existence of (100) and (200) reflections in the diffraction pattern proves that it is not a

200   rhombohedral unit cell, but a primitive hexagonal (Figure 9C). Therefore, the space group is

201   determined to be *P31c* (No. 159). The atom coordinates and symmetry equivalent positions of

202   the *d* superstructure are reported in Table 1.

203

204   The superstructure with cation sequence of Ca-Mg-Ca-Ca-Ca-Mg-Ca that was proposed to

205   explain the *d* reflections was referred to as δ structure (Wenk and Zhang, 1985; and Wenk et al.,

206   1991) (see Figure 9A for details). The calculated δ structure has slightly larger unit cell

207   parameters (a = 4.883Å and c = 16.281Å) than the *d* superstructure indicated here. The enthalpy

208   of a unit cell of δ structure is slightly higher than that of the *d* superstructure by 0.54 kJ/mol per

209   MCO_3 unit. The previously proposed δ structure is unstable with respect to the current *d*

210   superstructure. The proposed δ structure model was based on the assumption that overlapped

211   diffraction patterns from host dolomite and *d* superstructure were from the precipitates only

212   (Wenk and Zhang, 1985). Careful examination of their diffraction pattern (Fig. 1A of Wenk and

213   Zhang, 1985) and our FFT pattern (Figure 9D), show that the position of 003 is not half way

214   between 002 and 004 of the *d* superstructure, and the position of 009 is not midway between 008

215   and 0010 of the *d* superstructure. The *d* superstructure does not have reflections with odd *l* due to

216   its *c*-glide. A powder X-ray diffraction pattern with d_{104} value of 2.930Å for the *d* superstructure

217   is also calculated (Fig. 10).

218   The observed intermediate phases are analogous to those locally ordered domains in

219   mixed-layer clay minerals, such as interstratified chlorite/serpentine, chlorite/biotite, and

220   chlorite/pyrophyllite minerals (Banfield and Bailey, 1996; Xu and Veblen, 1996; Xu et al., 1996;

221   Wang and Xu, 2006). The observed intermediate phase between calcite and dolomite may be

222   described as interstratified calcite/dolomite, instead of δ–dolomite or d-dolomite.

223

IMPLICATIONS

225   The calculated energies of calcite (Ca(CO3)), dolomite (CaMg(CO$_3$)$_2$), and d superstructure

226   (Ca$_2$Mg(CO$_3$)$_3$) are 3620.64, 7132.37 and 10740.22 kJ/mol, respectively. The energy for the d

227   superstructure (Ca$_2$Mg(CO$_3$)$_3$) is higher (~4.2 kJ/mol per MCO$_3$ unit) than the sum of the

228   calculated energies from dolomite (CaMg(CO$_3$)$_2$) and calcite (CaCO$_3$) end members. The d

229   superstructures serve as a metastable phase with respect to the stoichiometric dolomite and

230   calcite. The d superstructures have a maximum of 4 repeats of Ca-Ca-Mg- along the c axis (<

231   35Å) in our sample and are only stable within dolomite host in the form of nano-precipitates. It

232   is very difficult for extra Ca ions in the dolomite structure to diffuse through carbonate layers

233   and to congregate to form lamellae parallel to the basal plane at low temperature (Wenk et al.,

234   1991; Shen et al., 2013). This explains all the reported occurrences of nano-precipitates of d-

235   reflections in natural samples. Wenk et al. (1991) summarized the various proposed

236   superstructures of Ca-Mg carbonates. By using Z-contrast imaging, we can image the cation

237   ordering directly and propose a more accurate structure model. By using the DFT method, we

238   can calculate the detailed structures and explore the energetics of these metastable nano-phases.

239   The methods may be applied to understand many other nano-phases, where there are challenges

240   or artifacts by using other methods.

241

245   **REFERENCES**

246   Aydinol, M., Mantese, J. and Alpay, S. (2007) A comparative *ab initio* study of the ferroelectric

247   behaviour in KNO_3 and $CaCO_3$. Journal of Physics: Condensed Matter, 49, 496210

248   Ayoub, A., Zaoui, A. and Berghout, A. (2011) High-pressure structural phase transitions and

249   mechanical properties of calcite rock. Computational Materials Science, 3, 852-857

250   Bakri, Z. and Zaoui, A. (2011) Structural and mechanical properties of dolomite rock under high

251   pressure conditions: A first principles study. physica status solidi (b), 8, 1894-1900.

252   Banfield, J.F., and Bailey, S.W. (1996) Formation of regularly interstratified serpentine –

253   chlorite minerals by tetrahedral inversion in long-period serpentine polytypes. American

254   Mineralogist, 81, 79-81.

255   Barnard, A. S. and Xu, H. (2008) An environmentally sensitive phase map of titania

256   nanocrystals. ACS NANO, 2 (11), pp 2237–2242.

257   Beran, A. and Zemann, J. (1977) Refinement and comparison of the crystal structures of a

258   dolomite and of an Fe-rich ankerite. Tschermaks mineralogische und petrographische

259   Mitteilungen, 4, 279-286

260   Chatterjee, S. and Saha-Dasgupta, T. (2010) First-principles simulations of structural, electronic,

261   and magnetic properties of vacancy-bearing Fe silicates. Physical Review B, 15, 155105

262   Frank, T.D. and Lyons, T.W. (1998) "Molar-tooth" structures: A geochemical perspective on a

263   Proterozoic enigma. Geology, 8, 683-686

264   Goldsmith, J.R., and Graf, D.L. (1958) Relation between lattice constants and composition of the

265   Ca-Mg carbonate: American Mineralogist, 43, 84-101.

266   Graf, D. (1969) Crystallographic tables for the rhombohedral carbonates. A correction. American

267   Mineralogist, 325

268   Kuang, H., Liu, Y., Peng, N., Luo, S., Li, J., Cen, C., and Chen, M. (2012) Molar-Tooth

269   Structure from the Mesoproterozoic Wumishan Formation in Lingyuan, Yanshan Region,

270   North China, and Geological Implications. Acta Geologica Sinica-English Edition, 1, 85-

271   95

272   Hossain, F., Dlugogorski, B., Kennedy, E., Belova, I. and Murch, G. (2011) First-principles

273   study of the electronic, optical and bonding properties in dolomite. Computational

274   Materials Science, 3, 1037-1042

275   James, N.P., Narbonne, G.M. and Sherman, A.G. (1998) Molar-tooth carbonates: shallow

276   subtidal facies of the Mid- to Late Proterozoic. Journal of Sedimentary Research, 5

277   Kirkland, E.J. (1998) Advanced computing in electron microscopy. Plenum Press, New York,

278   250 pp.

279   Kresse, G. and Furthmüller, J. (1996) Efficiency of ab-initio total energy calculations for metals

280   and semiconductors using a plane-wave basis set. Computational Materials Science, 1,

281   15-50

282   Long, D.G. (2007) Tomographic study of Paleoproterozoic carbonates as key to understanding

283   the formation of molar-tooth structure. Gondwana Research, 4, 566-570

284   Marshall, D. and Anglin, C. (2004) CO_2-clathrate destabilization: a new model of formation for

285   molar tooth structures. Precambrian Research, 3, 325-341

286   Meng, X. and Ge, M. (2002) The sedimentary features of Proterozoic microspar (Molar-tooth)

287   carbonates in China and their significance. Episodes-Newsmagazine of the International

288   Union of Geological Sciences, 3, 185-195

289   Oganov, A.R., Glass, C.W. and Ono, S. (2006) High-pressure phases of $CaCO_3$: Crystal structure

290   prediction and experiment. Earth and Planetary Science Letters, 1, 95-103

291   Pennycook, S. (2002) Structure determination through Z-contrast microscopy. Advances in

292   imaging and electron physics, 173-206

293   Pennycook, S., Rafferty, B. and Nellist, P. (2000) Z-contrast imaging in an aberration-corrected
294   scanning transmission electron microscope. Microscopy and Microanalysis, 04, 343-352

295   Perdew, J.P., Burke, K. and Ernzerhof, M. (1996) Generalized gradient approximation made
296   simple. Physical Review Letters, 18, 3865-3868

297   Pollock, M.D., Kah, L.C. and Bartley, J.K. (2006) Morphology of molar-tooth structures in
298   Precambrian carbonates: influence of substrate rheology and implications for genesis.
299   Journal of Sedimentary Research, 2, 310-323

300   Pratt, B.R. (1998) Molar-tooth structure in Proterozoic carbonate rocks: Origin from
301   synsedimentary earthquakes, and implications for the nature and evolution of basins and
302   marine sediment. Geological Society of America Bulletin, 8, 1028-1045

303   Reeder, R.J. (1992) Carbonates: growth and alternation microstructures. In P.B. Buseck, Eds.,
304   Minerals and Reactions at the Atomic Scale: Transmission Electron Microscopy, 27, p.
305   381-424. Reviews in Mineralogy, Mineralogy Society of America, Washington, D.C.

306   Reksten, K. (1990) Superstructures in calcian ankerite. Physical Chemistry of Minerals, 17, 266-
307   270

308   Shen, Z., Konishi, H., Brown, P.E. and Xu, H. (2013) STEM investigation of exsolution lamellae
309   and "*c*" reflections in Ca-rich dolomite from the Platteville Formation, western
310   Wisconsin. American Mineralogist, 4, 760-766

311   Sholl, D. and Steckel, J.A. (2011) Density functional theory: a practical introduction Wiley-
312   Interscience.

313   Stumm, W. and Morgan, J.J. (1995) Aquatic chemistry: chemical equilibria and rates in natural
314   waters. JOHN WILEY & SONS, NEW YORK, NY 10158(USA). 1995.

315   Van Tendeloo, G., Wenk, H. and Gronsky, R. (1985) Modulated structures in calcian dolomite:
316   A study by electron microscopy. Physics and Chemistry of Minerals, 6, 333-341.

317 Wang, Y., and Xu, H. (2006) Geochemical chaos: periodic and nonperiodic growth of mixed-
318   layer phyllosilicates. Geochimica et Cosmochimica Acta, 70, 1995-2005.

319 Wenk, H. and Zhang, F. (1985) Coherent transformations in calcian dolomites. Geology, 7, 457-
320   460

321 Wenk, H. and Zenger, D. (1983) Sequential basal faults in Devonian dolomite, Nopah Range,
322   Death Valley area, California. Science, 4623, 502-504

323 Wenk, H., Hu, M., Lindsey, T. and Morris Jr, J. (1991) Superstructures in ankerite and calcite.
324   Physics and Chemistry of Minerals, 6, 527-539.

325 Xu, H., and Veblen, D.R. (1996) Interstratification and other reaction microstructures in the
326   chlorite-berthierine series. Contribution to Mineralogy and Petrology, 124, 291-301.

327 Xu, H., Zhang, Y., and Veblen, D. R. (1996) Periodic and nonperiodic interstratification in the
328   chlorite-biotite series. American Mineralogist, 81, 1396-1404.

329 Zhang, F., Xu, H., Konishi, H., and Roden, E.E. (2010) A relationship between d_{104} value and
330   composition in the calcite - disordered dolomite solid solution series. American
331   Mineralogist, 95(11-12), 1650-1656.

332

Figure 1. (A)The outcrop shows the brittle deformation inside the carbonate layers with "molar tooth" structure. (B) Sinuous dark blue riboons of fine crystallined calcite ("molar tooth") exist in the dolomite host that is weathered into buff color. (C) Weathered surface of HHL-00H specimen . (D) "Molar tooth" becomes light color in fresh cut surface of HHL-00H specimen.
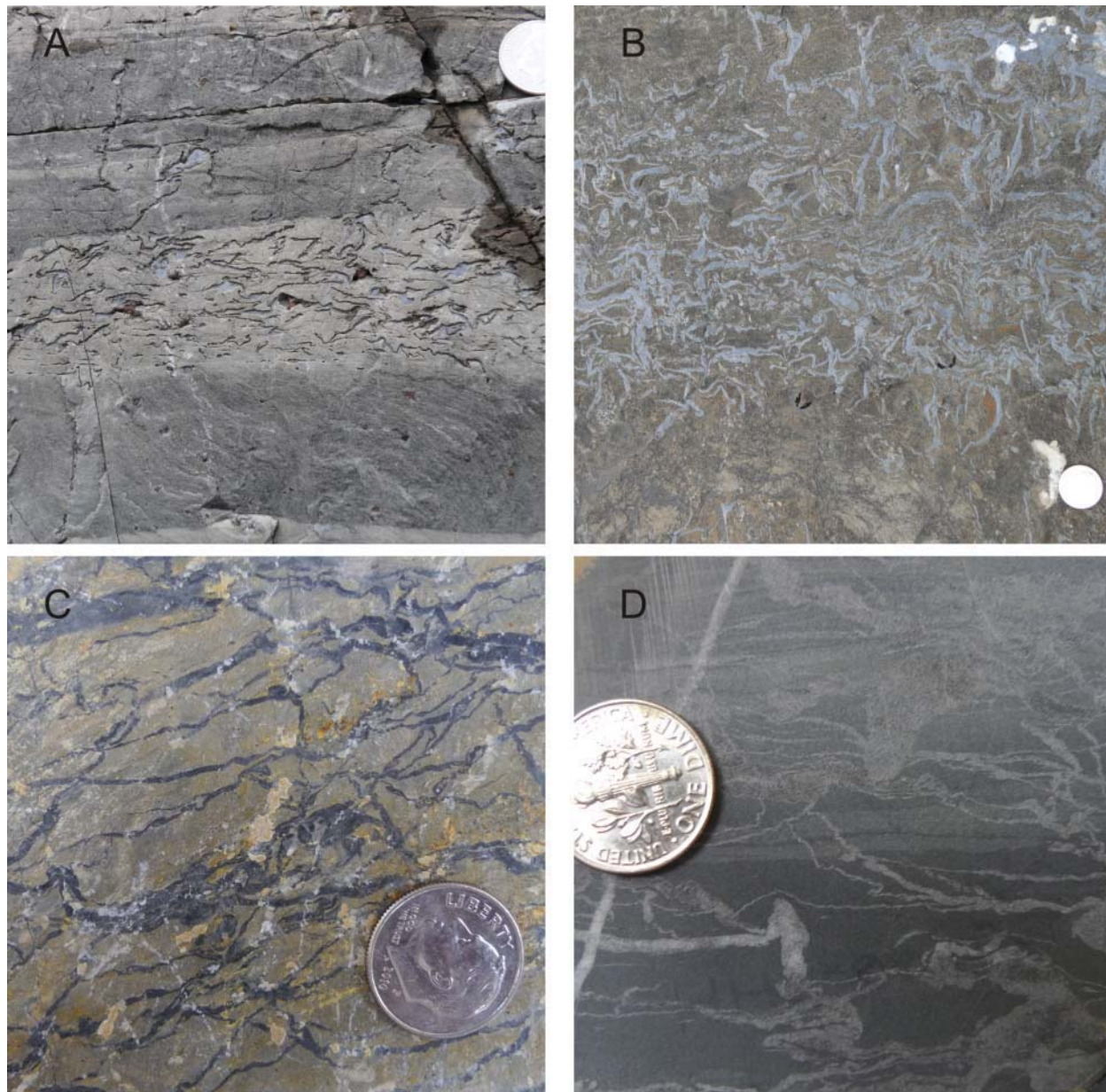
Figure 2. Powder XRD pattern of "molar tooth" host and "molar tooth" in sample HHL-00H.
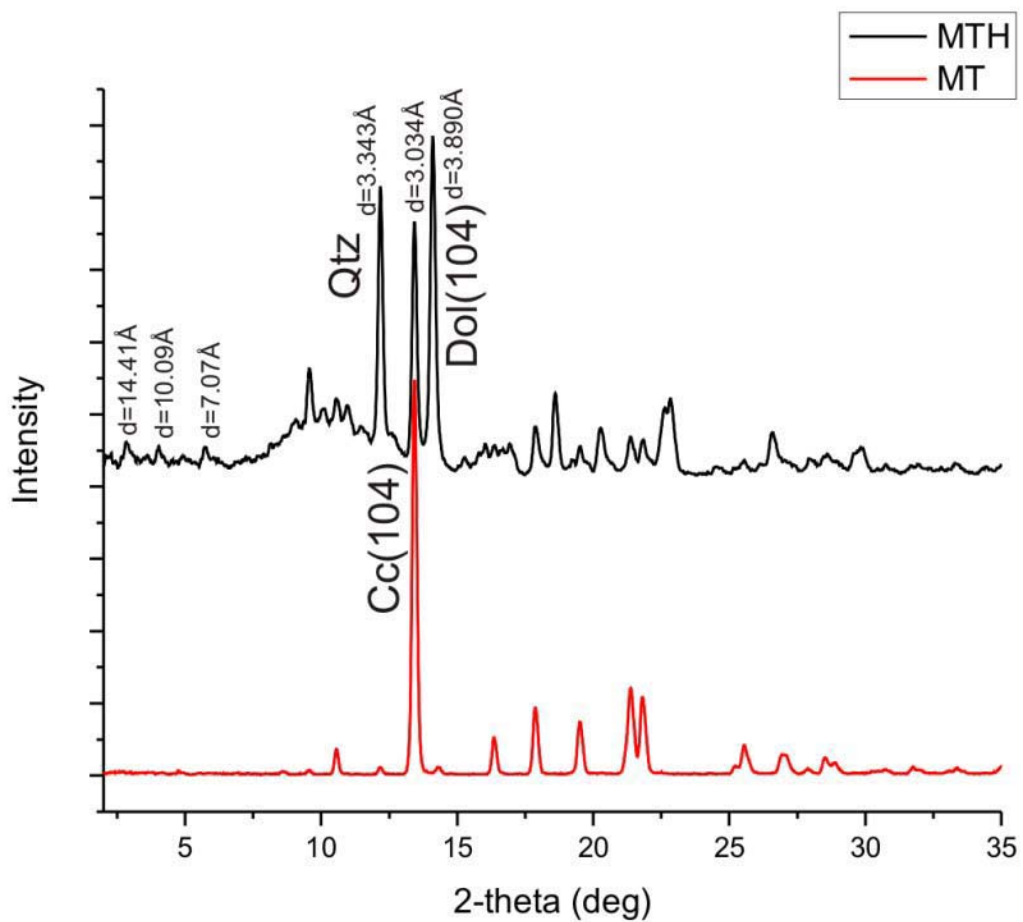
Figure 3. TEM image shows that calcite inclusion that is free of modulations or strain contrast in Ca-rich dolomite host.
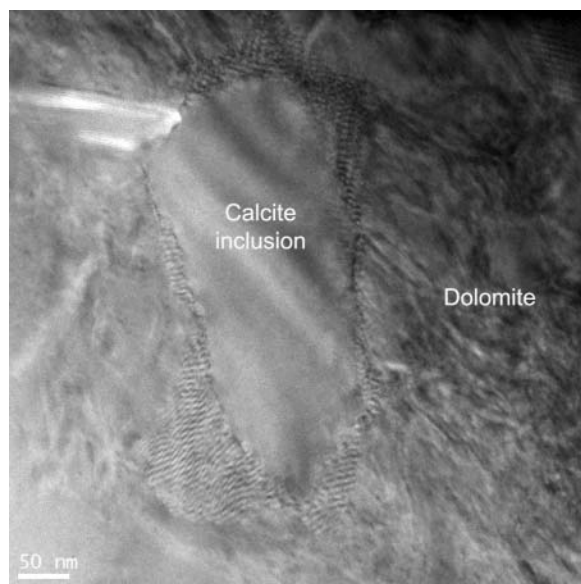
Figure 4. The diffuse streaks along $c*$ occur in the diffraction pattern of Ca-rich dolomite from Helena Formation, Montana. Some diffraction maxima occur at around 1/3 of d^*_{006}.
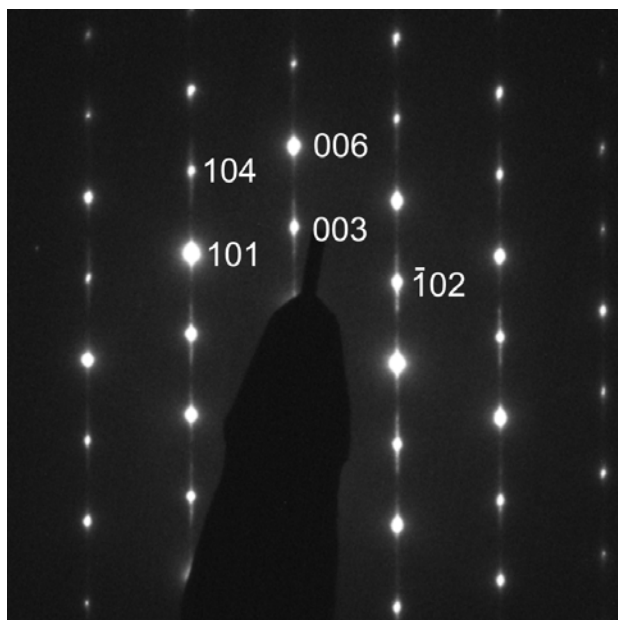
Figure 5. FFT patterns from TEM image show that the streaking and "*d*" reflections are from the precipitates (compare the FFT patterns from outlined areas of a and b).
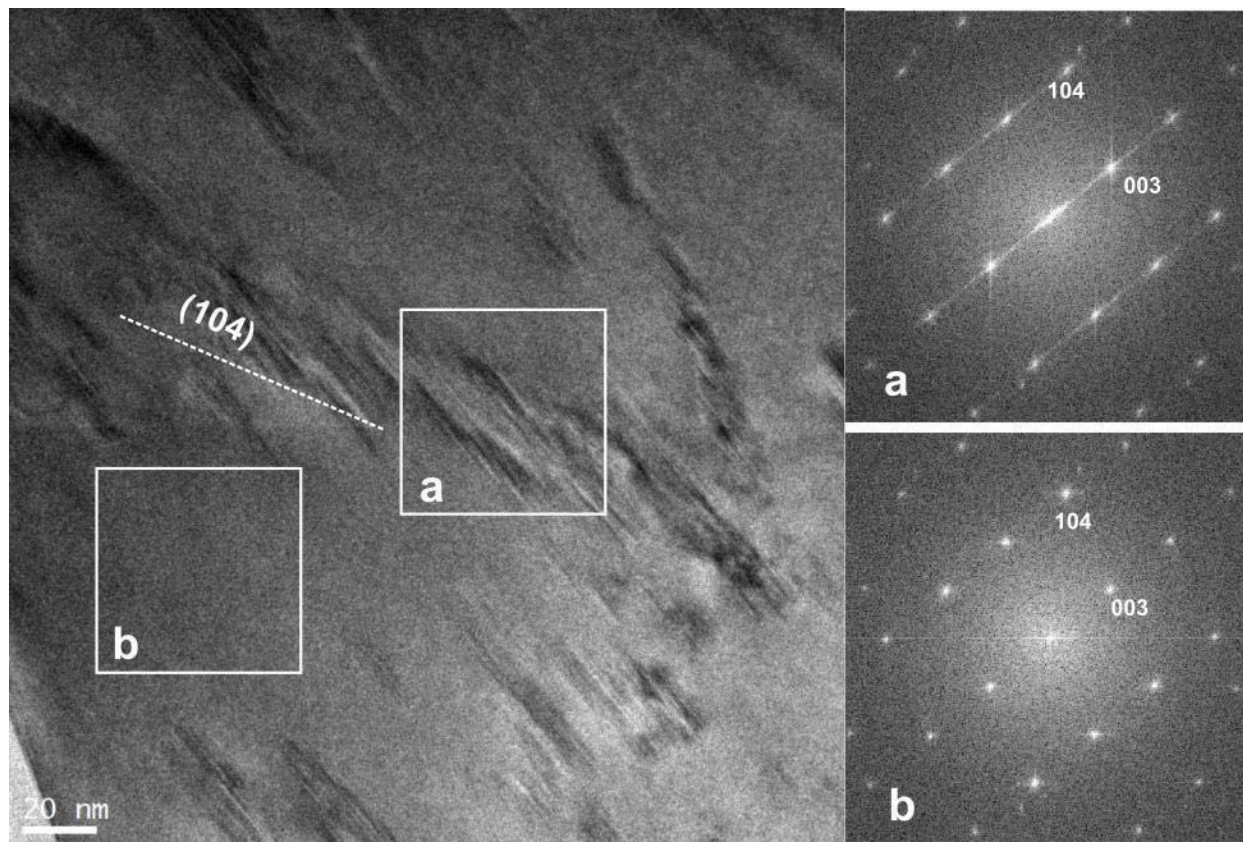
Figure 6. The dark areas of d superstructure in the bright-filed image (left) under STEM mode become bright in HAADF image (right), which means higher Ca content in the precipitates of d superstructure than the host dolomite.
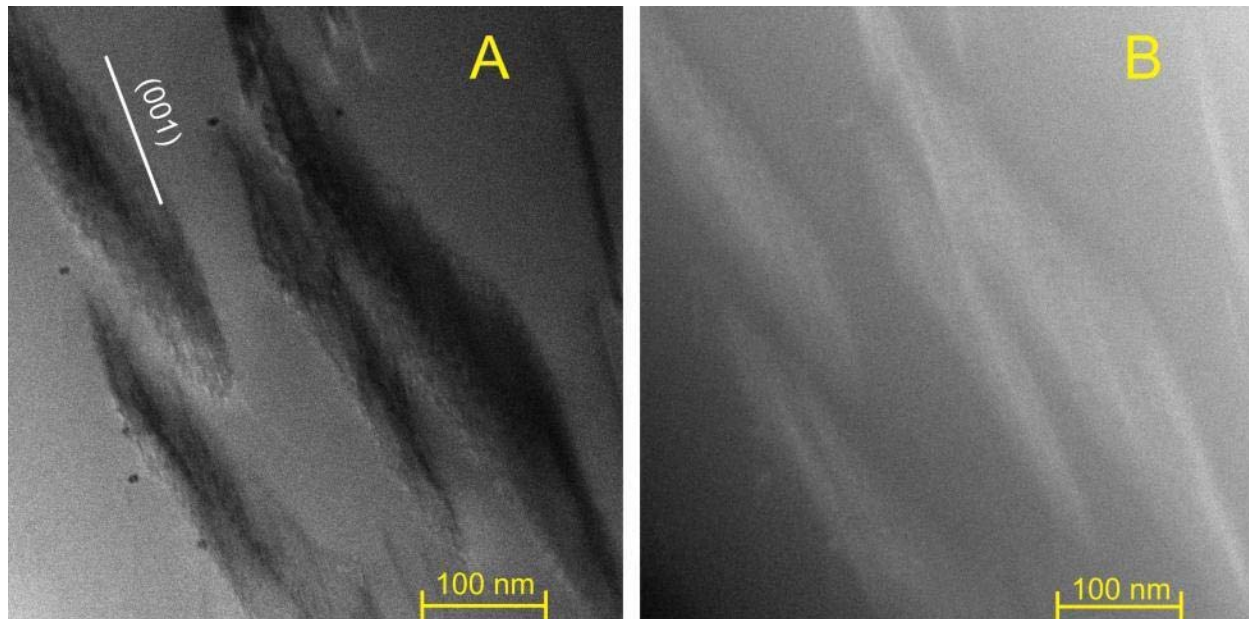
Figure 7. High magnification bright-field (A) and dark-filed (B) STEM images of *d* domains. Z-contrast (dark-filed) image shows that the Ca-rich precipitates have a cation sequence (bottom-right) of Ca-Ca-Mg-Ca-Ca-Mg- along *c* axis as opposed to dolomite cation sequence as shown in the middle-right corner (B). The occurrence of streaking and splitting along *c** (i.e., *d* reflections) in the FFT patterns (bottom-left corner). 003 and 009 spots are from host dolomite, not from the d superstructure, because the position of 003 half way between 002 and 004 of the d superstructure, and the position of 009 is half way between 008 and 0010 of the d superstructure. Noise-filtered Z-contrast image (C) shows enhanced cation sequences in the d superstructure and dolomite host. Line profiles from line 1 (dolomite host) and 2 (d superstructure) also illustrate the ordering of Ca and Mg atoms.
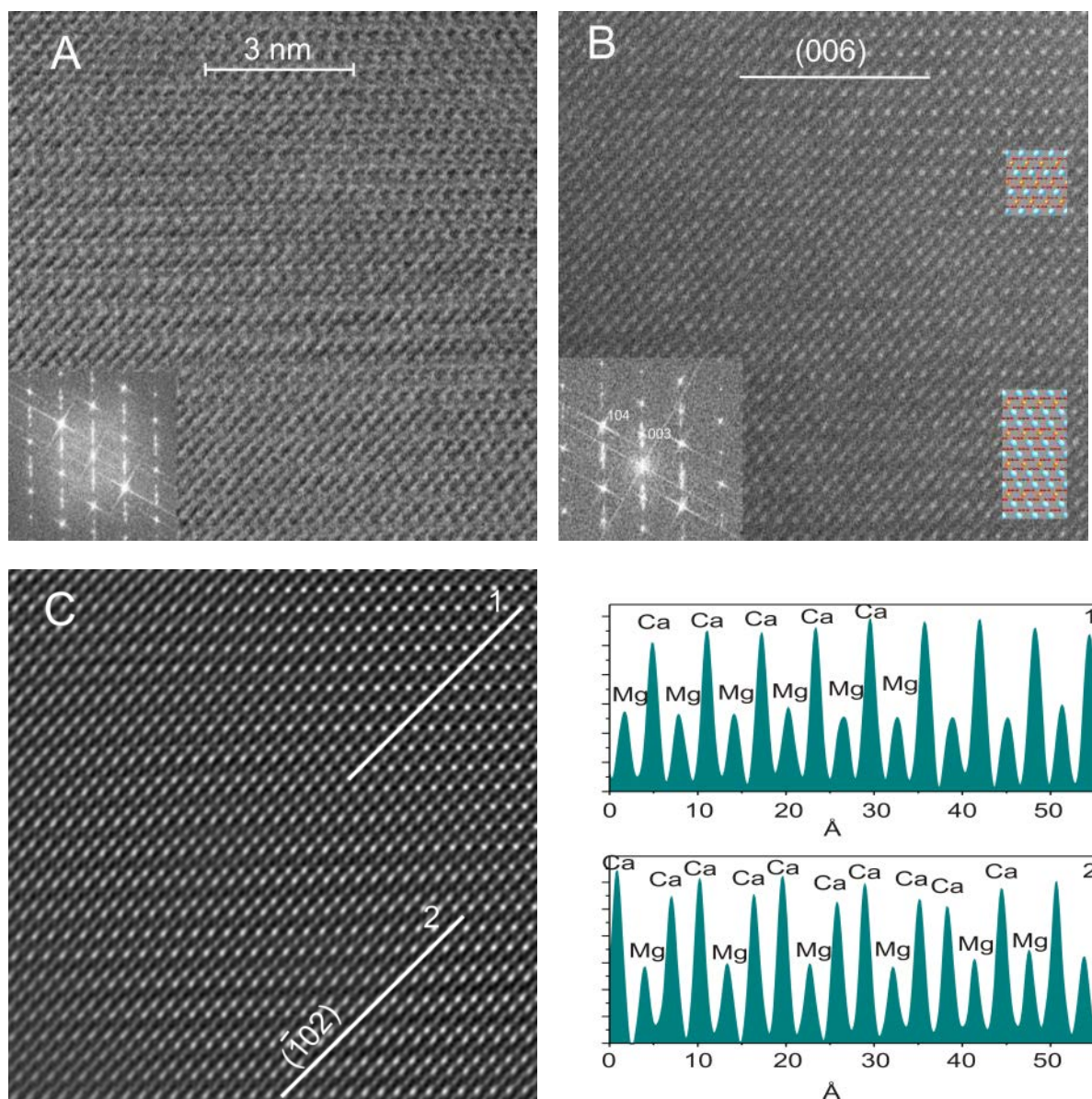
Figure 8. Z-contrast image shows calcite exsolution lamellae // (001) in dolomite host. The line profile 1 has six consecutive Ca columns along ($\bar{1}02$) trace. The line profile 2 of the dolomite region shows the normal dolomite cation sequence of alternating Ca and Mg columns. The line profile 3 shows one repeat of d superstructure. The lines with arrows show the boundaries between calcite and dolomite and between dolomite and d superstructure. The atomic models for dolomite/calcite and dolomite/d phase interfaces are shown at the bottom. Carbonate group are not shown proportionally in order to highlight the cations.
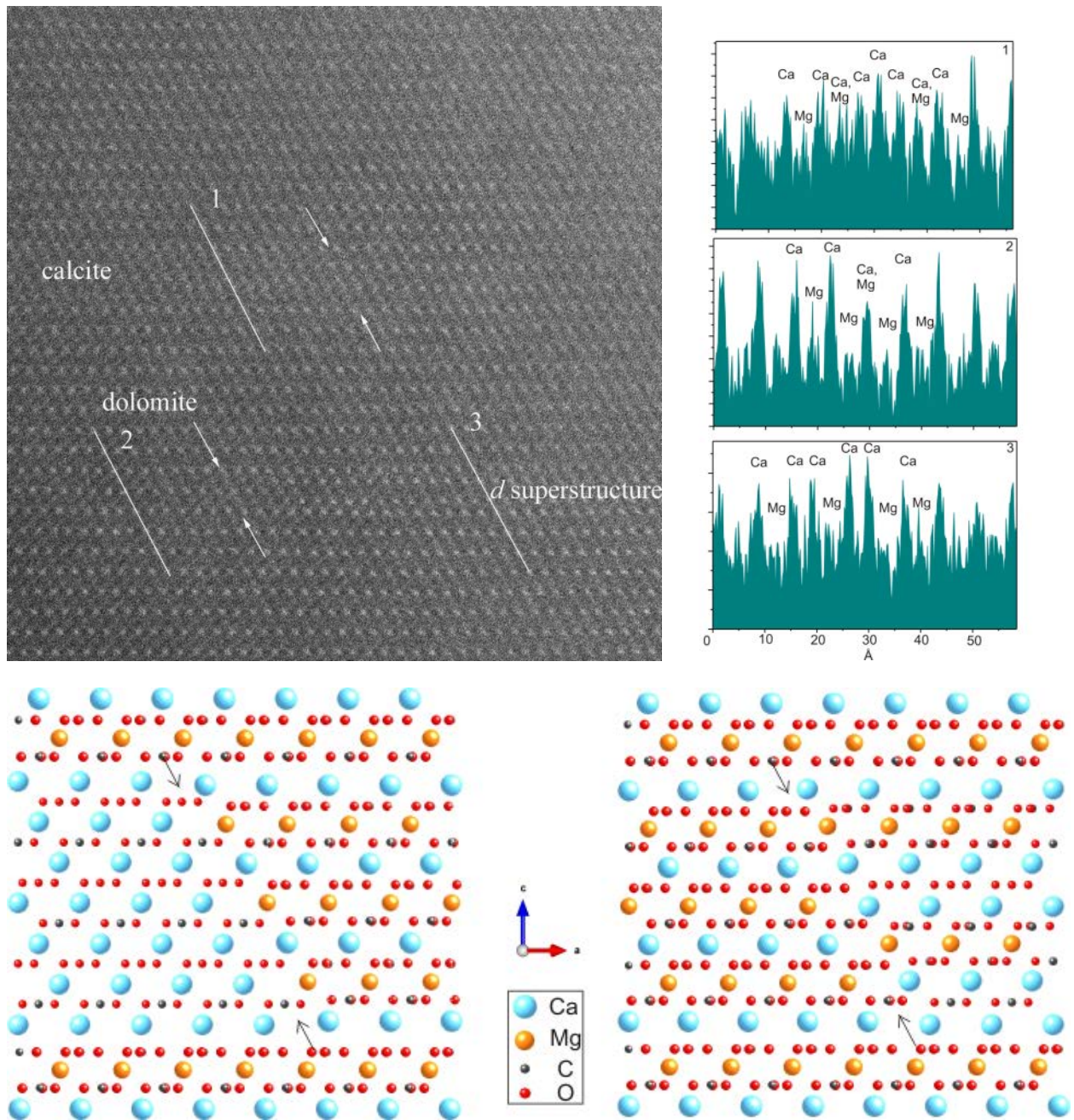
Figure 9. Previously proposed structure model for "δ dolomite" (A), and calculated model for *d* superstructure (B), and corresponding calculated electron diffraction pattern (C), compared to the FFT pattern (D) from an area dominated by the *d* superstructure. Very weak 003 and 009 reflections also occur in FFT pattern due to contributions from the dolomite host. However, the position of 003 is not half way between 002 and 004 of the d superstructure, and the position of 009 is not half way between 008 and 0010 of the d superstructure. The *d* superstructure does not have (*h0l*) reflections with odd *l* due to its *c*-glide.
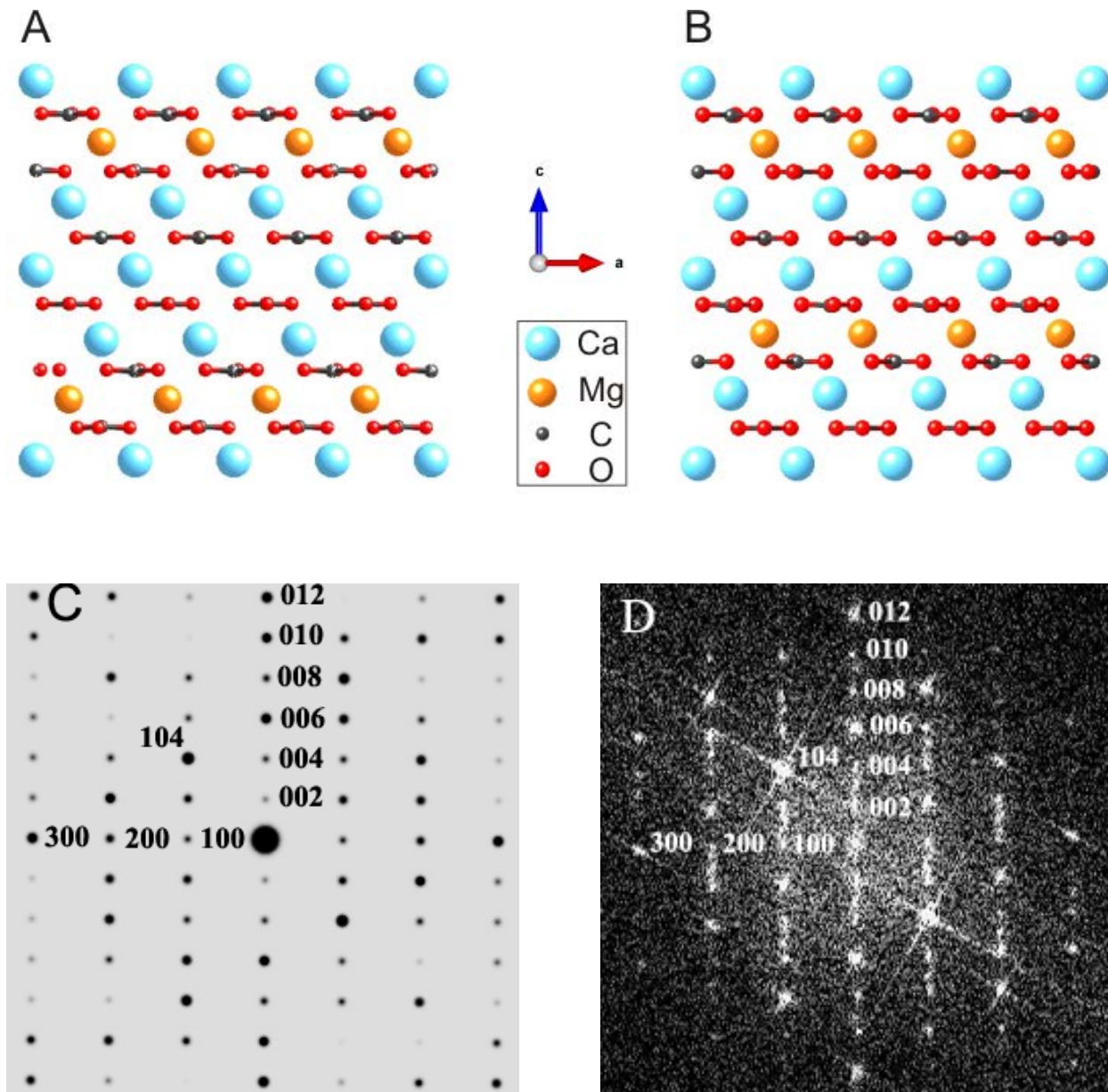
Figure 10: Calculated powder diffraction patterns of the *d* superstructure and stoichiometric dolomite (copper K-alpha radiation). The peak of (105) in dolomite does not appear in the *d* superstructure phase. However, the peak of (106) in the *d* superstructure phase does not appear in dolomite.
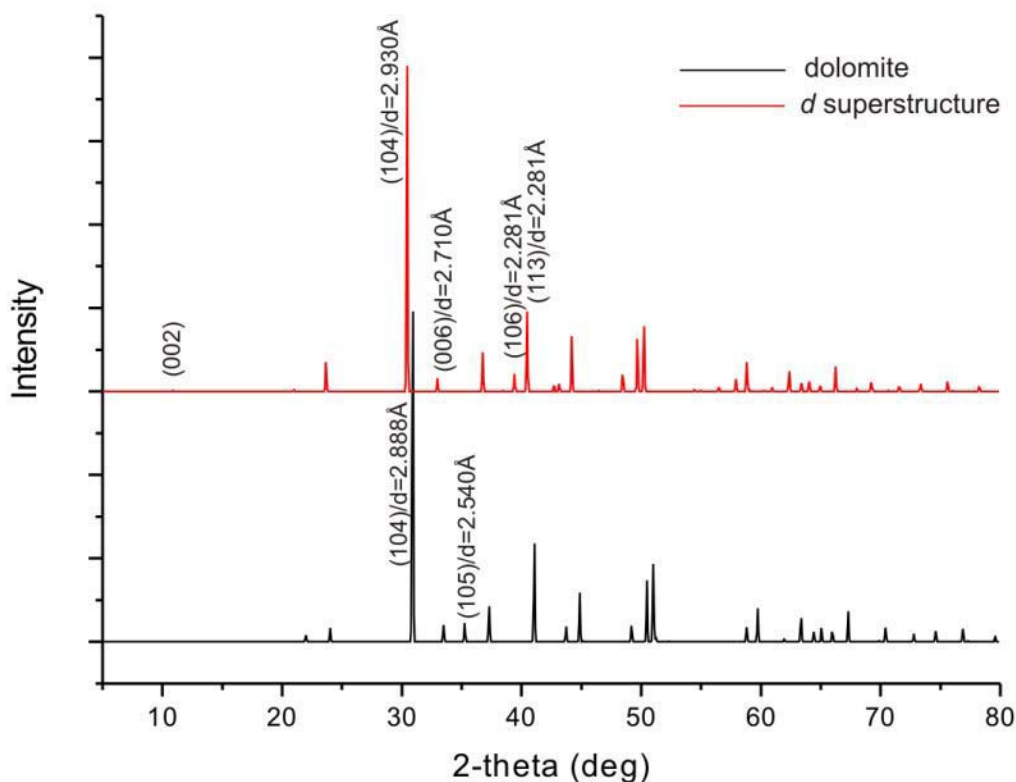
Table 1. Fractional coordinates of atoms, lattice parameters, and bond distances for the *d* superstructure calculated using DFT method.

Atom	x	y	z	Atom	x	y	z
Ca1	0.00000	0.00000	0.00000	Ca2	0.33333	0.66667	0.18457
Mg	0.66667	0.33333	0.34229	C1	0.66667	0.33333	0.09229
C2	0.00000	0.00000	0.26849	C3	0.33333	0.66667	0.41608
O1	0.66667	0.06803	0.09229	O2	0.28361	0.04018	0.26739
O3	0.04972	0.62648	0.41719				
a: 4.879Å *c*: 16.260Å **V:** 335.226Å^3				**Space group:** *P31c* (no. 159)			
C-O bond (Å) : 1.294, 1.297 **Ca-O bond (Å)** 2.355, 2.374 **Mg-O bond (Å)** 2.085							

Table 2. Calculated structural parameters of dolomite as compared to experimental and previously calculated data.

Lattice parameters	This work	Experimental	Theoretical
a (Å)	4.810	4.808[a], 4.812[b]	4.787[c], 4.877[d], 4.858[e]
c (Å)	15.704	16.010[a],16.020[b]	15.55[c], 16.285[d], 16.109[e]
V (Å^3)	314.611	320.504[a],321.251[b]	308.623[c],335.409[d],329.248[e]
C-O bond (Å)	1.294	1.233[a], 1.286[b]	1.286[c], 1.299[d]
Ca-O bond (Å)	2.358	2.405[a], 2.382[b]	2.328[c], 2.401[d]
Mg-O bond (Å)	2.069	2.114[a], 2.087[b]	2.071[c], 2.314[d]
O-Mg-O bond angles (°)	89.03, 90.97, 180	89.17, 90.83, 180[a]	89.335, 90.645, 180[c] 88.546,91.454,180[d]

[a] Graf ; [b] Beran and Zemann; [c] Hossain et al., LDA functional was used; [d] Hossian et al., GGA functional was used; [e] Bakri and Zaoui, fitted to Birch-Murnaghan equation of state.

Table 3. Calculated structural parameters of calcite as compared to experimental and previously calculated data.

Lattice parameters	This work	Experimental	Theoretical
a (Å)	4.995	4.990[a]	5.061[b], 4.981[c]
c (Å)	16.685	17.062[a]	17.097[b], 15.902[c]
V (Å^3)	360.435	367.916[a]	379.279[b], 341.676[c]
C-O bond (Å)	1.295	1.286[a]	
Ca-O bond (Å)	2.336	2.357[a]	

[a] Graf; [b] Ayoub, Zaoui, and Berghout; [c] Aydinol et al.